A&A 414, 717–726 (2004)
DOI: 10.1051/0004-6361:20031611

Astronomy & Astrophysics

Penumbral structure at 0.″1 resolution

I. General appearance and power spectra

L. H. M. Rouppe van der Voort⋆, M. G. Löfdahl, D. Kiselman, and G. B. Scharmer

The Institute for Solar Physics of the Royal Swedish Academy of Sciences, AlbaNova University Center, 106 91 Stockholm, Sweden
e-mail: rouppe,mats,dan,scharmer@astro.su.se

Received 16 April 2003 / Accepted 13 October 2003

Abstract. We analyse sunspot filtergrams of unprecedented quality obtained by Scharmer et al. (2002) with the Swedish 1-m Solar Telescope on La Palma. The observations comprise images in three different wavelength bands: 488, 436, and 430 nm (G-band). We find that there are still unresolved penumbral filaments which must have widths smaller than 80 km. The fine structuring along the filaments is limited. Penumbral grains have internal structure and look like they are split or crossed by narrow dark structures. We calculate intensity power spectra of the penumbra from images that are corrected for seeing using the Phase Diversity technique. The effects of high order aberrations that are not corrected for are estimated to be too low to be consistent with a flat power spectrum. The penumbral power spectra do not show any signs of bumps or peaks that could correspond to a preferred scale at 0.″35 for the width of penumbral filaments. We argue that the power spectrum is not a very reliable source of information concerning preferred scales.

Key words. Sun: photosphere – sunspots

1. Introduction

Sunspots consist of a dark central umbra surrounded, at least partly, by a filamentary penumbra. Smaller magnetic field concentrations (diameter <4 Mm) that fail to develop a penumbra (pores) are relatively short-lived as compared to sunspots, which can survive for weeks. Penumbrae can be considered to be an integrated part of sunspots, whose overall structure poses a basic problem which is still not completely understood (see, e.g., Thomas & Weiss 1992; Parker 1992; Schlichenmaier 2002; Thomas et al. 2002).

High-spatial-resolution observations are an important tool for discriminating between theoretical models and identifying the key physical processes, which, given the richness of fine-scale structures in the penumbra (reviews on penumbral fine-structure: Muller 1992; Sobotka 1997), are likely to take place on small spatial scales. So far, the spatial resolution achieved with state-of-the-art instrumentation has proven to be insufficient to resolve the smallest building blocks of the penumbra. Asymmetric spectral line profiles indicate a high degree of unresolved structuring, both along the line-of-sight (i.e., vertical structuring) and laterally. For example, models developed to explain asymmetric Stokes profiles in the penumbra incorporate magnetic flux tubes with widths smaller than 150 km (Solanki & Montavon 1993; Sánchez Almeida 1998; Martínez Pillet 2000; Müller et al. 2002), a spatial scale which has been beyond the limit of the best observations.

Although single filtergrams miss the spectral information required to derive information on the magnetic field, bulk velocities or vertical structuring, they are ideally suited to scrutinize the lateral sizes of penumbral fine-structure because of the advantage of a higher spatial resolution as compared to spectrometric observations. Specific questions that can be addressed concern the size distribution of penumbral filaments and, notably, whether there is a lower limit to the filament width and if they have a characteristic scale.

Scharmer et al. (2002) estimated the resolution of their sunspot observations to be better than 0.″12 (≈90 km), improving the spatial resolution with a factor of about 2 as compared to earlier sunspot observations. These observations show new kinds of small-scale structures in solar magnetic regions, the most interesting being that many penumbral filaments, notably those protruding into the umbra, contain dark cores. This phenomenon is still lacking an explanation, but demonstrates that there is substructure in what may hitherto have been seen as a single penumbral filament. A dark-cored filament also seems to be a coherent structure, indicating that the penumbra is not a random mass of dark and bright filaments at these scales.

This paper uses images from the data set of Scharmer et al. (2002) to further explore the fine structure of the penumbra of

Send offprint requests to: L. H. M. Rouppe van der Voort,
e-mail: rouppe@astro.uio.no

⋆ *Present address:* Institute of Theoretical Astrophysics, Oslo University, PO Box 1029 Blindern, 0315 Oslo, Norway.

a large sunspot close to disk centre. The main part is a discussion of the power spectra of the structures in relation to the earlier work, at lower spatial resolution, of Sánchez Almeida & Bonet (1998) and Sütterlin (2001). Before that, we describe the general appearance of the penumbral structures from visual inspection of the images.

2. Observational data

The data of Scharmer et al. (2002) analysed here consist of a set of images taken in three wavelength bands. The target was NOAA active region 10030 which was close to disk centre (N 19.6, E 7.0, $\mu = 0.96$) on 15 July 2002, and observed between 10:33 and 15:05 UT. In this paper we concentrate on the best images, the results are based on three sets of exposures obtained between 11:33 and 11:37 UT, and one set at 13:20 UT.

The three filters used were a wide blue-green filter centred at 488 nm, and two narrow-band filters centred on the G-band and on the nearby continuum. The G-band is often used in solar observations because it highlights small magnetic flux concentrations (e.g., Berger et al. 1995; Muller & Roudier 1984). Technical details for the images are presented in Table 1.

The observations were made with the Swedish 1-m Solar Telescope (Scharmer et al. 2003a). Since the spatial resolution of small-scale structure is the issue here, it is worth stating in some detail how the seeing effects are countered. This is done with three complementary methods. The incoming wavefronts are flattened by an adaptive optics (AO) system (Scharmer et al. 2003b) consisting of a tip/tilt mirror and a 19-electrode bimorph mirror, the latter controlled using measurements from a 19-micro-lens Shack–Hartmann wavefront sensor. The tip/tilt and AO systems are designed to correct 15 low-order Zernike modes (2–15 and 19 as numbered by Noll 1976). There are therefore always residual higher-order aberrations in the images. The second method is frame selection (Scharmer 1989) which means that the images with highest contrast in small-scale structures during an adjustable selection interval (usually between 15 s and a couple of minutes) are stored to disk while the rest are discarded. Finally, the selected images can be post processed with image-reconstruction techniques.

In this study, we use different post-processing techniques (see last row of Table 1). The most simple one is deconvolution using a modulation transfer function (MTF) that is computed assuming an ideal telescope and including known properties of the detector. The G-band images were also restored using the technique of phase diversity (henceforth "PD", see Löfdahl & Scharmer 1994; Paxman et al. 1992a; Gonsalves 1982). Thus simultaneous exposures (on the same CCD) were made with a known focus difference. This allows them to be jointly processed in order to estimate both the unknown object and the unknown phase aberrations. Recently, Löfdahl (2002) developed a new code, capable of Joint Phase Diverse Speckle (JPDS) processing (Paxman et al. 1992b), which was used for these data. Löfdahl & Scharmer (2003) describe the detailed procedure to JPDS reconstruct a G-band image in this data set from four PD pairs of exposures, although the data used here were restored with a different setting of some parameters. The processing was performed on 128×128-pixel subfields ($5.''25 \times 5.''25$), in order to account for anisoplanatism. Wavefront phases were estimated as expansions in atmospheric Karhunen–Loève modes 2–36, implemented as sums of Zernike polynomials (Roddier 1990). The subfield size is slightly smaller than what was used by Löfdahl et al. (1998, 2001) for data collected with the 47.5-cm Swedish Vacuum Solar Telescope (SVST). This makes sense with respect to the more severe anisoplanatism expected with a larger aperture and with the higher order wavefront expansion used here. We did not attempt to find the optimum size, that may well be even smaller.

Table 1. Observational details. MTF ≡ MTF-deconvolved, PD ≡ phase-diversity restored. Pixel size $0.''041$. $1'' = 734$ km, 100 km = $0.''14$. The KAF4200 and KAF1600 CCDs from Eastman Kodak sit in Megaplus 4.2 and Megaplus 1.6 cameras, respectively.

filter	488	G-cont	G-band
$\lambda_{\rm filter}$ ($\Delta\lambda_{\rm fwhm}$) [nm]	487.7 (8)	436.4 (1.1)	430.5 (1.2)
exposure time [ms]	13	5	6
CCD	KAF4200	KAF1600	KAF1600
field of view [″]	82×83	62×41	26×40
post processing	MTF	MTF	MTF or PD

Figure 1 shows part of the 488-nm image with the field of view (FOV) for the PD-restored image indicated. Also indicated are examples of subfields which are used for quantitative analysis. Subfields from the PD-restored image are shown magnified and with individual intensity scaling in Fig. 2.

3. Inspection of penumbral structures

3.1. Different passbands

Figure 3 shows a part of the penumbra as seen through the three filters. The G-band is displayed twice: PD-restored for the very highest resolution as well as MTF-deconvolved in the same way as the other two passbands to allow for a comparison with them. The latter image is the best of the four exposures that go into the PD reconstruction. Note that the images are recorded close in time but not so close so as to have the same distortion by seeing, so a pixel to pixel comparison is not possible. From this comparison we can conclude that the same structures are visible in all passbands. The PD-restored G-band image shows the highest contrast and the smallest details, which is expected from its more advanced processing.

Table 2 shows the mean RMS contrast for the subfields of Fig. 1. Apart from the obvious fact that the PD-restored G-band image shows the highest contrast, it is clear that the G-band images have higher penumbral contrast than the nearby continuum. At 488 nm the contrast is still lower which is partly because of the longer wavelength (less temperature-sensitive Planck function and slightly lower resolution).

Even though the G-band contrast is highest, we do not consider the scene there to be significantly different from that in the other bands. We conclude that the PD-restored G-band image – which has the highest resolution – is representative of penumbral structure.

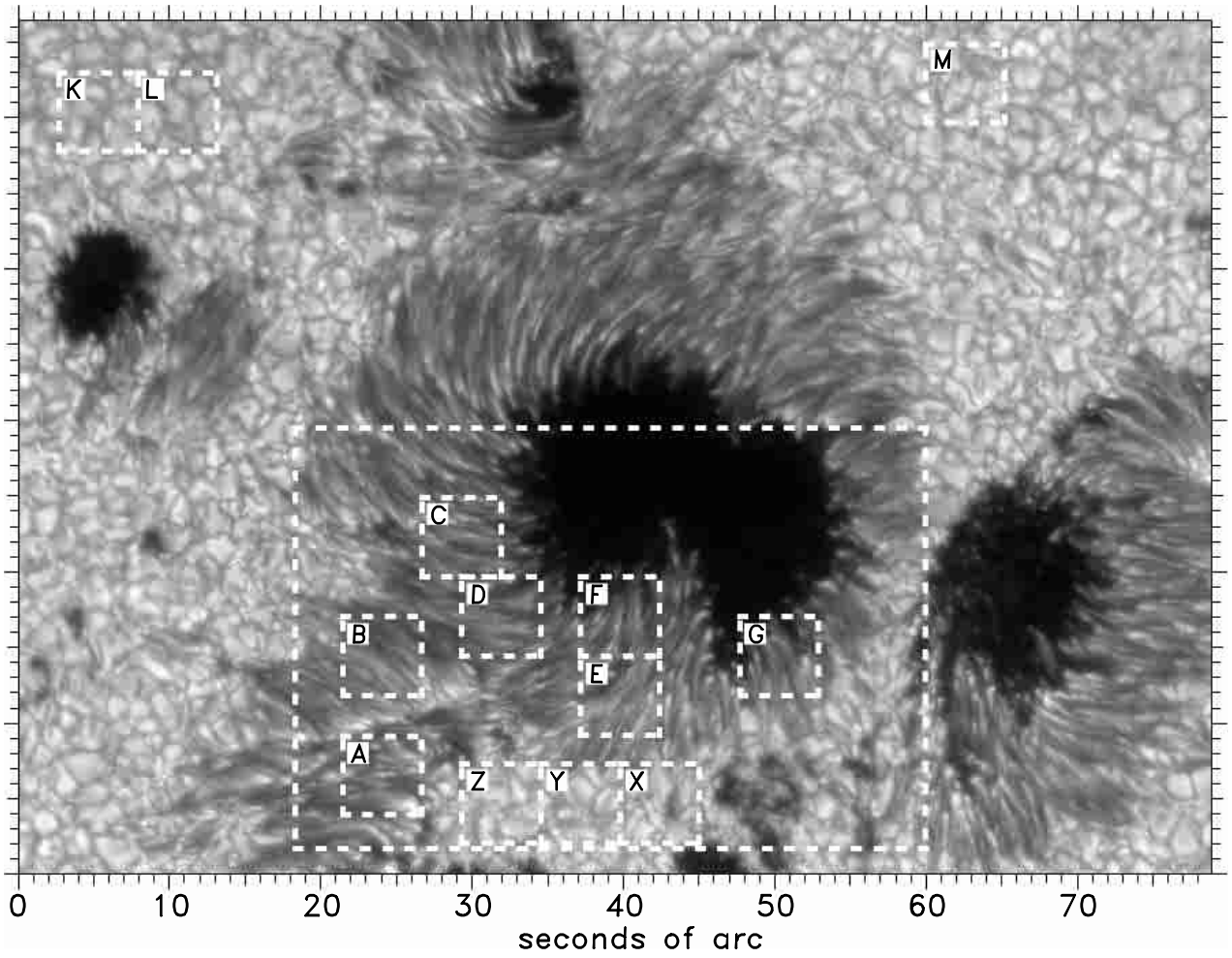

Fig. 1. The largest sunspot of AR10030 in the 488-nm image. The large box indicates the field-of-view of the PD-restored G-band image. The smaller boxes represent example subfields that are used for quantitative analysis. A–G: penumbra, K–M: quiet granulation, X–Z: active granulation. See also Fig. 2 and Table 2.

Table 2. RMS contrast in the different bands. Mean values for penumbra (A–G), active granulation (X–Z) and quiet granulation (K–M, only in 488 nm).

filter	488	G-cont	G MTF	G PD
penumbra (A–G) [%]	13.1	14.9	19.0	21.5
active granulation (X–Z) [%]	7.9	11.0	12.0	13.4
quiet granulation (K–M) [%]	7.0	–	–	–

3.2. Filament dimensions

The penumbral scene in Fig. 3 shows the typical mass of filamentary structure. Whether filaments should be considered as bright on a darker background or vice versa is controversial. Most studies agree that the bright and dark filaments are such only in a local context (see, e.g., Muller 1992; Tritschler & Schmidt 2002). In his review paper, Sobotka (1997) describes the penumbra as being formed by "bright filaments separated by narrow dark fibrils".

The current images, representing an advance in almost a factor of two in resolution, do not immediately challenge this view when one only looks in the main part of the penumbra. The dark-cored filaments, however, which are so common in Fig. 3, could be the typical constituent part of the whole penumbra even if the confusion in the penumbra away from the umbral border may hide the pattern.

Figure 4 shows two representative parts of the penumbra, each together with an intensity tracing. The plots also show the theoretical diffraction-limited point spread function (PSF; marked D in the figure) and an illustration of the Rayleigh criterion. A comparison of these curves and the intensity tracing clearly tells us that many bright and dark features are so narrow that they must be unresolved. Since their widths are almost as small as the FWHM of the PSF, the width of the corresponding solar features cannot be larger than a resolution element (about 80 km, see Sect. 4.2). Note, however, that there are resolved features, both dark and bright.

Obviously, the increase in resolution shows that what is considered as one penumbral filament at lower resolution actually consists of several narrower components. Note that the fine structure along their length is limited. The intensity along filament varies smoothly until it fades (sometimes to apparently reappear further on) or until it seemingly runs in another filament. But most structures are filamentary at this resolution and

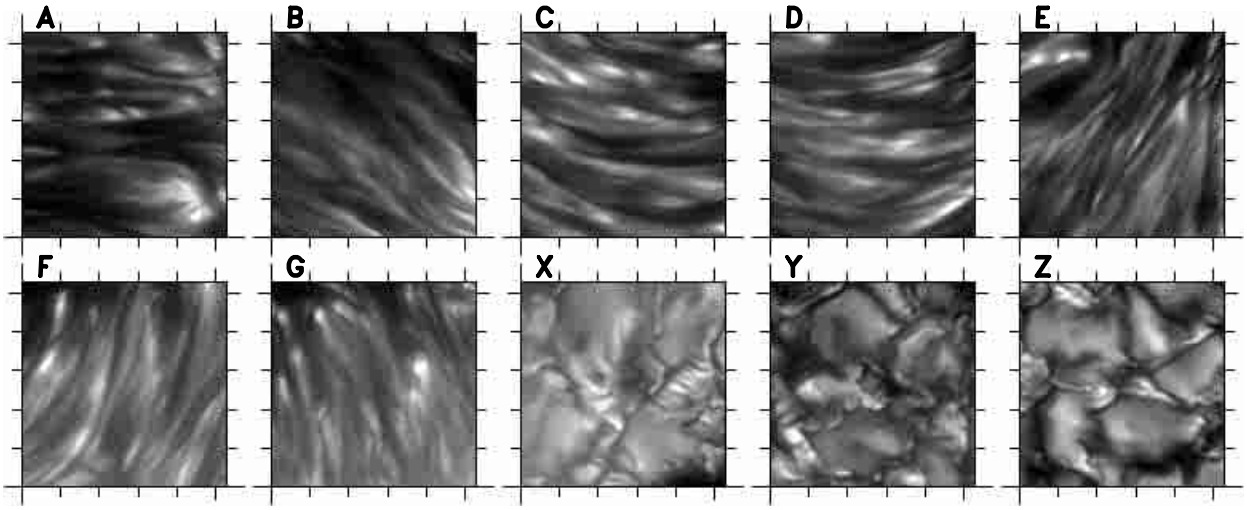

Fig. 2. The penumbral and active granulation subfields indicated in Fig. 1, but from the PD-restored G-band image and individually scaled for best contrast. Tick marks have 1″ spacing.

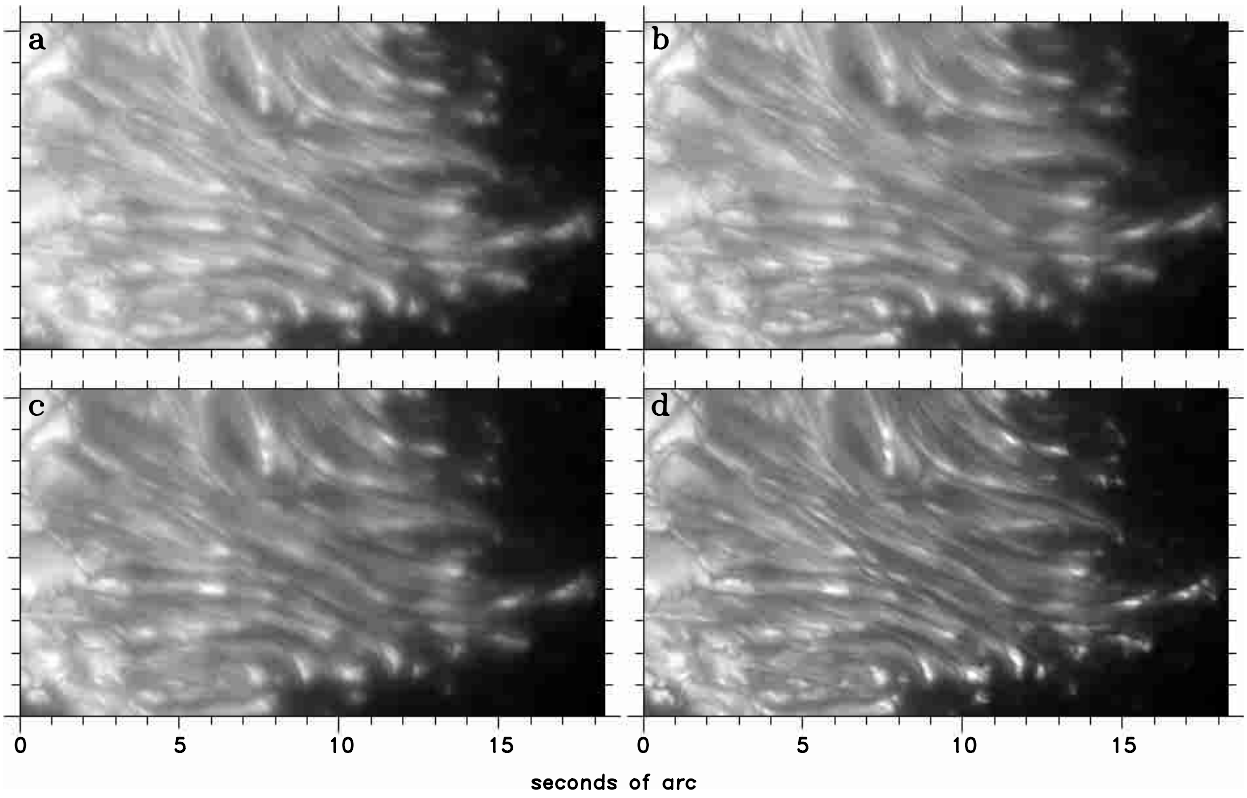

Fig. 3. Part of the penumbra in three wavelength bands. **a)** 488 nm, **b)** G-cont, **c, d)** G-band. **a)**, **b)** and **c)** are MTF-deconvolved. **d)** is PD-restored.

do not break up in other patterns. A possible exception to this are the "twisted" filaments noted by Scharmer et al. (2002), but the interpretation of bright filaments being composed of chains of aligned grains (Muller 1973b) does not seem to be appropriate at this resolution.

The maximum length of the filament is difficult to measure. Due to their fading and reappearing, they can be difficult to track as individual filaments. Some examples of rather long filaments, with lengths 5″–9″(3600–6600 km), are displayed in Fig. 5.

3.3. Penumbral grains

Penumbral grains are localised brightenings in a penumbra, situated at the end of bright filaments closest to the umbra. They are dynamical objects (e.g. Sobotka et al. 1999; Sobotka & Sütterlin 2001) which, for the inner penumbra, are seen moving inward towards the umbra (Muller 1973a) – this is not likely to represent a flow of gas but the movement of a pattern. In the simulations of Schlichenmaier et al. (1998a,b), a penumbral grain is the site where the hot part of a rising flux tube crosses the photosphere.

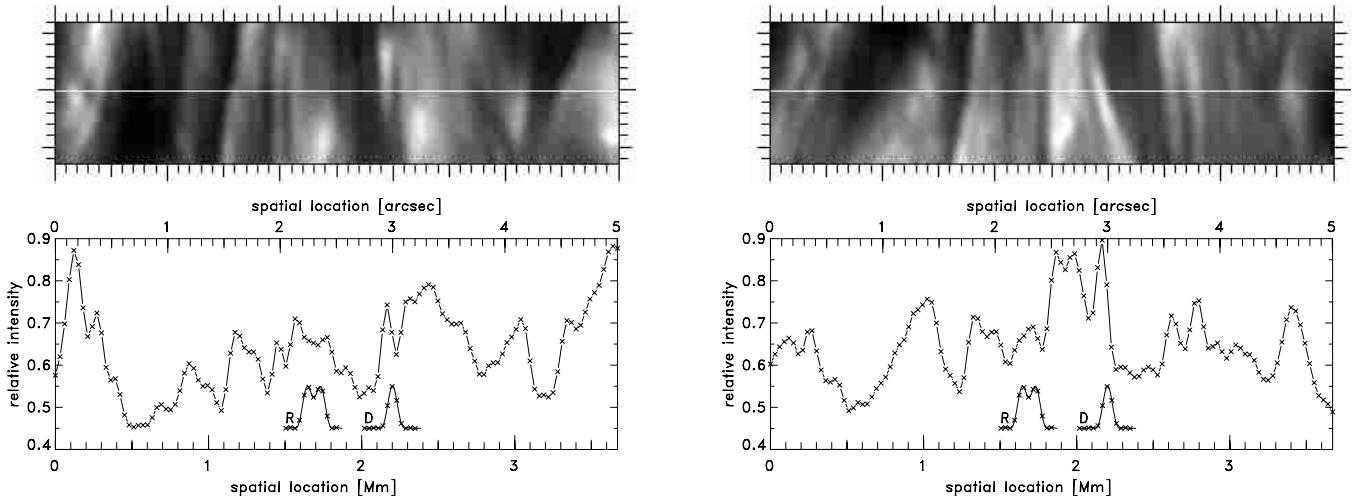

Fig. 4. Penumbral intensity tracings from a PD-restored G-band image. D shows the theoretical diffraction-limited point-spread function of the telescope as a cut through an Airy function with a FWHM of 0.″092, the diameter of the first dark ring being 0.″113. R illustrates the Rayleigh criterion for resolution. There are apparently many unresolved peaks and dips in the curves.

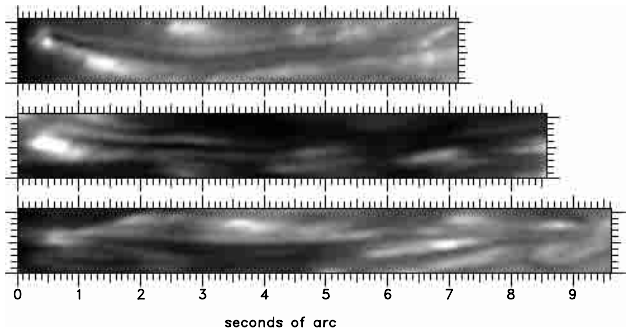

Fig. 5. Sample long filaments from PD-restored G-band images.

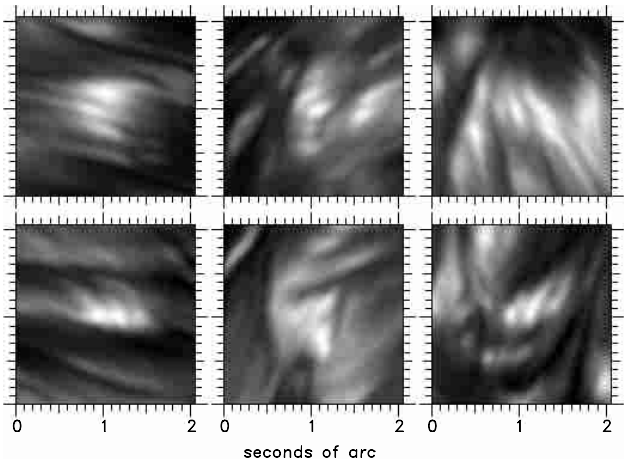

Fig. 6. Sample penumbral grains from PD-restored G-band images.

Figure 6 shows features that at lower resolution would be classified as penumbral grains. It is clear that these have internal structure. Each consists of several bright patches, and many show narrow dark structures that appear to run through them. The penumbral grains appear to be coherent structures and not random assemblies of brighter spots.

4. Power spectra

Several earlier studies tried to determine a characteristic penumbral-filament width by direct measurement of photometric profiles (see, e.g., Muller 1973b; Bonet et al. 1982). However, measuring penumbral-filament dimensions directly in images is a subjective operation and therefore other, more objective methods have been employed to address this question. We will here discuss the Fourier amplitude and power spectra of the penumbral structures. We will compare our results with those of Sánchez Almeida & Bonet (1998, henceforth SAB98) and Sütterlin (2001, henceforth S01). They also studied sunspots close to disk centre but used telescopes with less than half the aperture, the 47.5 cm SVST and the 44-cm Dutch Open Telescope (DOT), respectively. SAB98 analysed observations in the continuum at 525.7 nm, while S01 used observations in the G-band.

It should be noted that the sunspot of this study was a large, rotating spot while those of the two cited papers were smaller with radially oriented penumbral filaments. We proceed with the comparison while keeping this difference in mind. We hope to be able to return to the question of differences in penumbral fine-structure between individual sunspots in a coming paper.

4.1. Methods

We compute power spectra in two dimensions (2D) mainly because the 1D (semi-)circular tracings used by SAB98 and S01 are impractical for such an irregularly shaped penumbra as in our target sunspot. This should not be any concern for the smaller scales, except for a slight averaging effect. Also, SAB98 obtain similar results with 2D spectra as with their 1D method. It must be noted, however, that our spectra are constrained to high spatial frequencies due to the limited size of the subfields, approximately $5'' \times 5''$, and the necessary apodization.

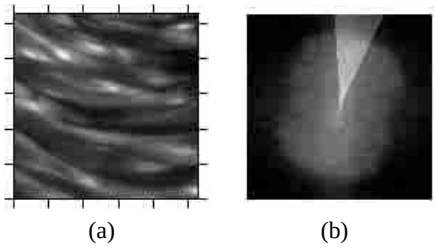

Fig. 7. a) PD-restored G-band image of penumbral subfield C. **b)** 2D power spectrum. The highlighted 30° sector is in the direction of maximal power and is used for calculating the 1D spectrum.

With penumbral power we understand in the following that the power is measured in the direction perpendicular to the filaments. Figure 7 illustrates the method we use. Figure 7a shows a penumbral subfield. This image is first normalized to the mean intensity in the granulation subimages X, Y, and Z and then used to compute the 2D power spectrum shown in Fig. 7b. The direction perpendicular to the filaments is determined by finding the maximum power along an azimuthal tracing at 90% of the diffraction limit. The 90% radius was determined by trial and error. The evaluation has to be done at high spatial frequencies, because it is the rapidly varying filamentary structures that define the direction of the penumbra. At the same time it has to be at low enough frequencies that there is still signal to be measured above the noise. Within a 30° sector, as indicated by the highlight in the image, we then calculate an azimuthal average 1D spectrum from the same data, but inverse filtered without noise suppression (see Appendix). Note that the averaging means that the power we obtain is not the maximum but rather a representative value. The characteristic direction found in the subfield of the G-band PD-image was used to calculate the 1D spectra in the corresponding subfields of the other filtergrams. The fact that filaments curve notably in some of the subfields also has the effect of reducing the power from a possible maximum. Comparison between the different subfields indicates that the degree of curvature present in the selected subfields does not result in a significant difference in the slope of the different power spectra.

The lin–log plot in Fig. 8 shows power spectra for the subfield in Fig. 7 as observed in the different wavelength bands as well as different states of reconstruction of the G-band data. They are noisy in the low-frequency part because of the limited field of view and the narrowing of the sector used for azimuthal averaging. In the high-frequency part, the unprocessed data shows how the signal power is drowned by the flat white noise at a level of about 2×10^{-6}. The upturn of the power spectra of the MTF- and PD-restored data represents this noise, amplified by division with MTFs that are almost zero close to the diffraction limit.

Ignoring the noise-dominated parts, the different curves compare as expected from the contrast values of Table 2. The PD-reconstructed G-band data have the most power followed by the MTF-deconvolved G-band. The two continuum MTF-deconvolved curves are similar and the unprocessed G-band data have the least power, particularly at high spatial frequencies.

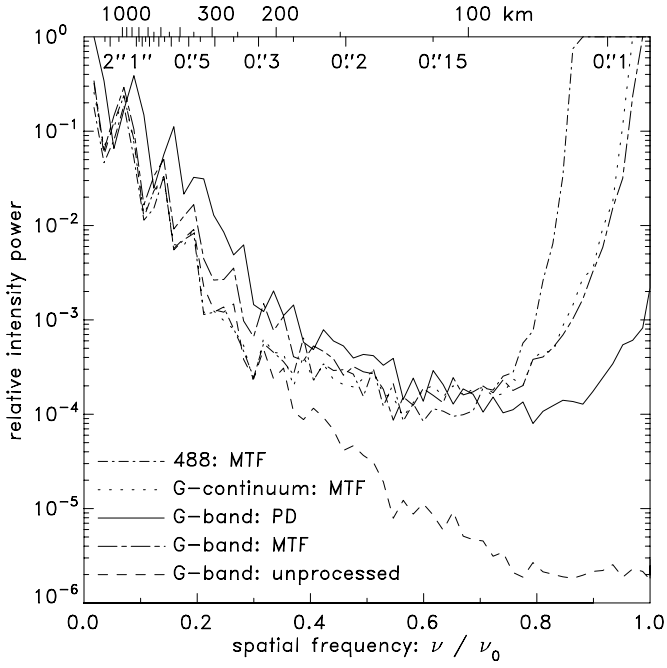

Fig. 8. Power spectra of the penumbral subfield C from Fig. 7. The deconvolution has been made without noise suppression. The axes are lin–log. ν_0 is the diffraction limit at 430 nm (G-band).

4.2. Spectral slope

SAB98 note that their penumbral amplitude spectra very nearly coincide with the atmospheric MTFs measured by Bonet et al. (1995) from the edge spread function of the lunar limb during a solar eclipse (also using the SVST but on a different occasion than their sunspot observation). Since the Fourier transform of the data is equal to the object transform times the MTF, they suggest that the object spectrum is flat, i.e., constant with spatial frequency. On the contrary, S01 finds a spectrum with a definite slope from his speckle-reconstructed data.

In Fig. 9 we show power spectra based on our PD-restored G-band data for active granulation and across penumbral filaments. These curves are smoother than those in Fig. 8 because they are averages of power spectra from several different subfields. Neither spectrum is flat. They extend to higher spatial frequencies before turning up, partly for the same reason but mostly because we have subtracted the expected contribution from the noise, see the appendix. Both curves extend to beyond 0.8 times the diffraction limit, corresponding to a resolution of approximately 0.″11 or 80 km.

For comparison, the plot also shows corresponding spectra for the data in the earlier papers. The curve corresponding to the data of SAB98 is based on an exponential fit to the signal dominated part of the amplitude spectrum (their Fig. 2), which is very nearly linear in their lin–log plot[1]. The slope of this curve can be compared to our spectra but the vertical offset of the curve is not known. Because their data are uncorrected for seeing, this curve is expected to be below the other curves but by how much is uncertain. An additional offset in the

[1] Our spectra in Fig. 8 are not well approximated by exponentials, which is why we use log–log in the following figures.

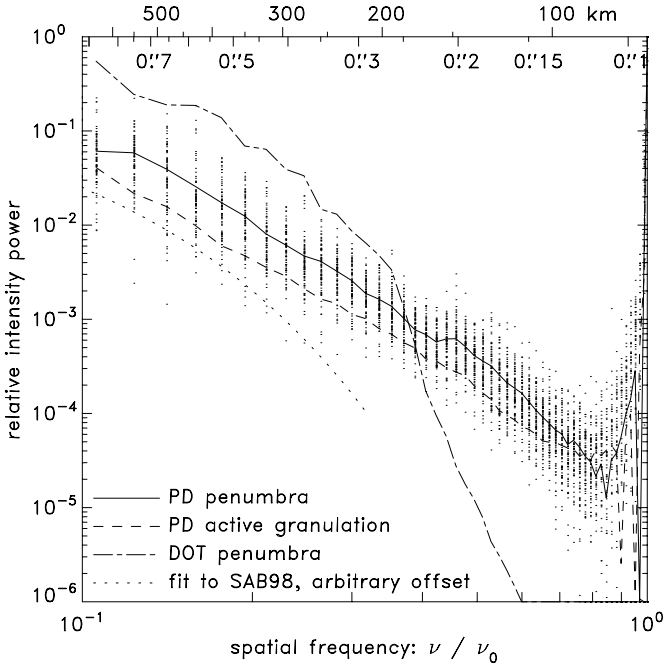

Fig. 9. Log-log plots of noise-corrected G-band power spectra. Each dot represents data for one of several partly overlapping penumbral subfields selected from four of our best PD-restored frames (see e.g., A–G in Fig. 2). The solid line represents the running mean for all the subfields. The long-dashed curve is calculated in the same way from the active granulation subfields (e.g., X–Z). In total, 20 granular and 80 penumbral subfields were included. The DOT curve was computed from the noise-filtered data of S01. The shortest-dashed curve represents a fit to the results of SAB98 – its position along the vertical axis is arbitrary. ν_0 is the diffraction limit at 430 nm (G-band).

same direction can also be expected due to the lower contrast at longer wavelengths. The DOT curve is an average power spectrum computed by us from three penumbral subfields from the speckle-reconstructed DOT G-band data of S01, which were kindly made available to us by Dr. P. Sütterlin. The latter spectra were calculated with the same method as for our own data (except for noise correction because the data are noise filtered) normalizing the penumbral intensity to the mean intensity of the surrounding granulation.

We first comment on the spectrum of SAB98, which is based on data that are not corrected for any blurring effects. The authors caution that the curve should not be trusted below 0.″4. Indeed, above that point, the slope agrees well with our data, while the power rapidly falls off at smaller scales due to seeing effects and the smaller aperture. The question is whether effects unaccounted for in our reconstructed data are enough to require a flat spectrum or if the MTFs of Bonet et al. (1995) just happen to coincide with their power spectra. The latter hypothesis is possible, since their MTFs lack instantaneous information pertaining to the actual moment of observation. They also suffer from the circular symmetrical approximation necessary when measuring possibly strongly asymmetric 2D MTFs using the 1D information in the edge spread function. The MTF shown in log scale in Fig. 10a is an example. This MTF is calculated from the PD estimated wavefront corresponding to one of the four focused images in the PD data set used to restore subfield C in Fig. 7a. In Fig. 10b, the square of all four MTFs for the focused images, in the direction perpendicular to the filaments (averaged in the same sector as the power spectra, see Fig. 7b), are shown. The variation is small at some spatial frequencies and almost an order of magnitude in others, and this should affect the slope of the power spectra of individual data frames. Note that these MTFs correspond to four exceptionally good images collected within a few seconds and with very similar contrast. The variation would be even larger between images of different quality. On the other hand, the MTFs of Bonet et al. (1995) do include systematic effects from the detector, from atmospheric scattering, and from high order aberrations not included in the truncated expansion of the wavefront used in our PD procedure, see Sect. 2. In the following we estimate how much these shortcomings of our methods influence our resulting power spectra.

In Fig. 11 we demonstrate by simulation for different seeing conditions, how the MTF is affected by the uncorrected higher modes as well as some residual low order modes. The latter effect is due to cross talk between modes of different order in both the AO systems and in the PD processing. For each indicated value of the Fried parameter r_0, 100 random wavefronts were generated from a modified Kolmogorov distribution. The modification, which should correspond to a conservative approximation of the AO and PD corrections, is that the variances for all low order Karhunen–Loève modes (mode number <28) were set to the variance of mode 28, i.e., the correction is assumed to be to the same level as the uncorrected tail. The quadratic average of the MTF corresponding to each wavefront is plotted in Fig. 11. These curves consist of two parts. At low spatial frequencies (outside the plot window) they are seeing limited, decreasing rapidly. In the mid and high frequency range, they are similar to the diffraction-limited curve but suppressed with an approximately constant factor that varies with r_0. These MTFs are similar to the simulations of Nisenson & Barakat (1987). Figure 11 also shows a squared model detector MTF (Stevens & Lavine 1994) of the KAF1600 CCD at 430.5 nm.[2] Figure 12 shows multiplicative corrections for these two effects, that could be applied to the PD-corrected power spectra, depending on r_0. It is clear that they are far from being steep enough to make our spectra flat, for any realistic seeing condition (as well as some unrealistic ones).

We turn now to the DOT data of Fig. 9. At low frequencies the DOT power spectrum runs approximately parallel to our penumbral curve but at a factor of about 4 higher. From a knee at about 0.″35, it becomes slightly steeper. The parallel shift can be explained by the fact that, while the AO system and the PD processing correct a finite number of wavefront modes, speckle interferometry imposes Kolmogorov atmospheric statistics on the estimated PSFs. So the speckle reconstruction already includes the effects of high-order tails shown in Fig. 11, which are not corrected for in our PD-reconstructions. The factor 4 corresponds approximately to the correction for $r_0 = 15$ cm

[2] The KAF4200 pixels are identical to the KAF1600 pixels, although at 487.7 nm the MTF at the diffraction limit is a couple of percent lower than at 430.5 nm.

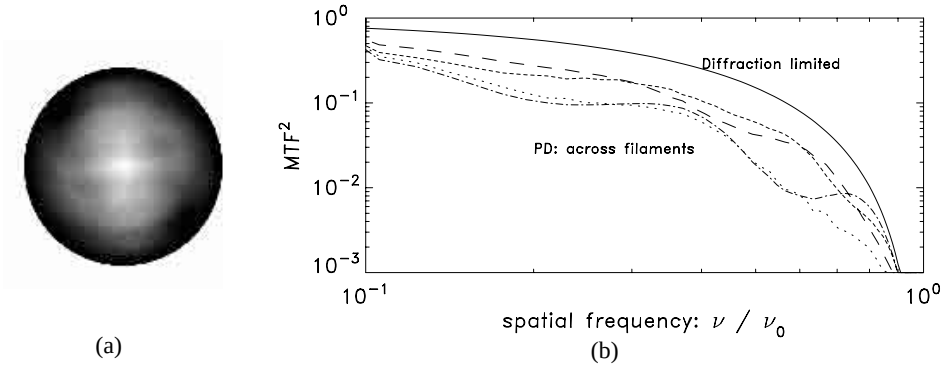

Fig. 10. PD MTFs. **a)** One of the four MTFs estimated with PD corresponding to the subfield in Fig. 7a (circle indicates diffraction limit). **b)** Squared sector averaged MTFs for the four focused images in the PD data used to make the image in Fig. 7a. Diffraction-limited MTF^2 plotted as a reference. The spatial frequency coordinate is normalized to the diffraction-limited frequency at 430 nm.

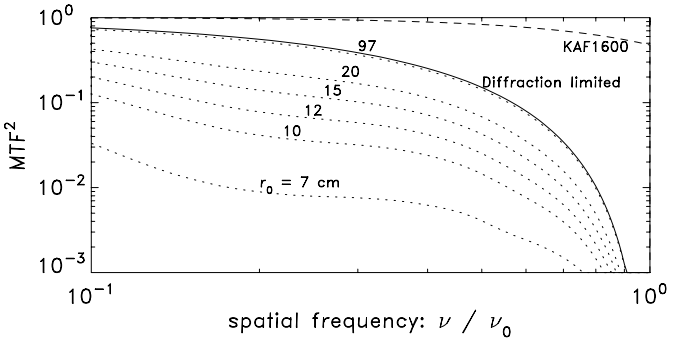

Fig. 11. Squared simulated MTFs corresponding to the tail of uncorrected modes for different seeing conditions. Diffraction-limited MTF^2 plotted as a reference. Also, the MTF^2 of the KAF1600 CCD detector is plotted. ν_0 is the diffraction limit at 430 nm (G-band).

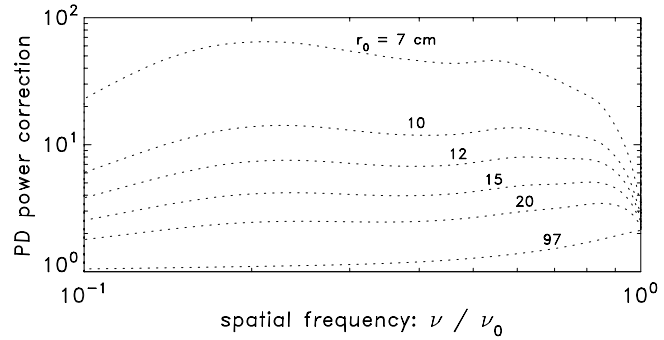

Fig. 12. Power spectra corrections for PD reconstructed data: squared ratio of the diffraction-limited MTF to the combined MTF of the detector and uncorrected high-order atmospheric modes. ν_0 is the diffraction limit at 430 nm (G-band).

seeing. Löfdahl & Scharmer (2003) find that the estimated wavefronts for these data are consistent with $r_0 \approx 20$ cm, although this is a very approximate value, which ignores distortions of the statistics by frame selection and field-dependent AO correction. The exact numbers are not important, since the simulation is only meant to illustrate the type of effect involved.

A remaining uncertainty is the effect of atmospherically scattered stray light, which is unaccounted for by PD and speckle methods alike but would be included in the direct limb measurements of Bonet et al. (1995). However, it seems that most studies of that problem conclude that its contribution to the PSF have an effective width of on the order of at least 30″ (e.g. Chae et al. 1998, Fig. 4). This produces a slowly varying bias and is unlikely to have any influence on the power spectrum at these small scales.

This discussion has highlighted the uncertainty surrounding the true shapes of power spectra of small solar structures. Even so, it is clear that the uncertainties are not large enough to make our data consistent with a flat spectrum. In fact, both the low frequency part of the DOT data and our own PD data power spectra (corrected as appropriate) fit well to power laws, ν^α. The active granulation seems to have a slope of $\alpha \approx -3.6$, while the penumbral power is steeper with $\alpha \approx -4.0$.

4.3. Preferred sizes

S01 finds an excess in penumbral power as compared to quiet granulation and he claims that the excess peaks at 0.″35, which has been considered by observers to be a typical width of penumbral filaments (Sobotka 1997).

Figure 13 shows a similar comparison between penumbral and granular spectra. As in Fig. 9, our spectra fit well to power laws. The G-band PD FOV only shows granulation which is fairly magnetically active. We therefore compare the power of penumbra, active granulation and “quiet granulation” (at least more quiet) in our 488-nm images, which has a larger FOV, (see Fig. 1). In contrast to the PD restorations and the speckle restorations of S01, this image was restored only for the theoretical MTF of the telescope and detector. This is spatially invariant, so the deconvolution could be performed with the same low-pass filter over the whole image. It should be noted that the residual wavefronts are larger in the quiet granulation subfields, because they are further away from the FOV of the AO wavefront sensor.

In Fig. 13, we also see the penumbral power excess, but as our spectra continue smoothly to higher frequencies, there is no apparent preferred scale of any curve at 0.″35. In fact, they all look like power laws all the way to the noise dominated regime.

We suggest that the 0.″35 peak of S01 is an artifact from field-dependent low-pass filtering during the

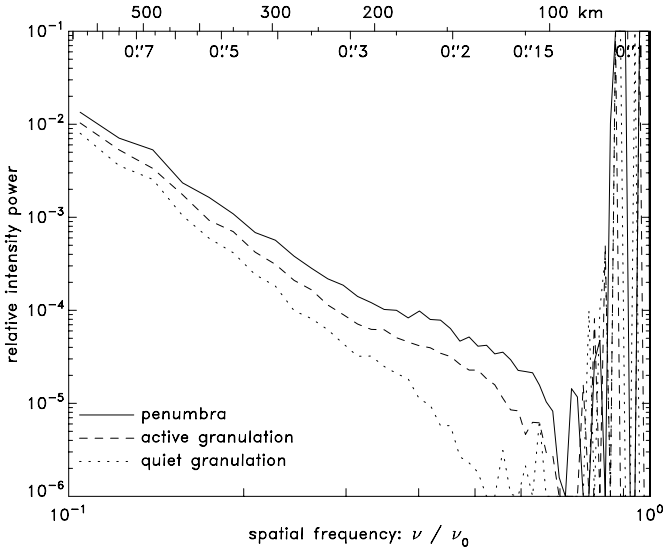

Fig. 13. Mean power at 488 nm for 47 penumbral, 12 active-granulation, and 6 quiet-granulation subfields from 3 frames. ν_0 is the diffraction limit at 430 nm (G-band).

image-reconstruction process. Although the seeing statistics can be assumed to be similar over a large FOV during the collection of a 100-image speckle data set, which would argue for similar filtering of the entire FOV, the extent of the signal-dominated domain does not only depend on the seeing but also on the object. E.g., it is not unlikely that the high-contrast G-band filigree boosts the power at high frequencies enough to extend the signal-dominated regime, so that this power drops later. Indeed, comparison of the power spectra in Fig. 13 shows that for our data, the penumbral and active granulation power spectra are signal dominated at higher frequencies than the quiet granulation.

4.4. Discussion

As noted in Sect. 3.2 there are still many unresolved features at the current resolution limit and it should be noted that the non-flatness of the power spectra is not an argument per se against the existence of the km-sized filaments inferred by SAB98. On the contrary, power laws with $\alpha \approx -2$, common in the power spectra of natural images (images of trees, landscapes, natural textures, etc.), can be attributed to a scale invariance with an approximately constant energy content per decade (Field 1987). Also, turbulence is known to generate power spectra that fall off with the similar slope of $\alpha \approx -5/3$. However, as demonstrated quite drastically by Nordlund et al. (1997), even an $\alpha \approx -2$ power law is no guarantee for turbulence, scale invariance or structures at all sizes. They show that the power spectrum of (simulated) granulation is also close to an $\alpha \approx -2$ power law, where the high-spatial-frequency power comes exclusively from the sharp edges between granules and intergranular lanes. Also, if one would dare to extrapolate our steeper $\alpha \approx -3.6$ and $\alpha \approx -4.0$ power laws, they may put some constraint on the smallest structures.

There is a small peak at 0.″2 for the penumbral data in Fig. 9 and maybe a corresponding, weak feature for the active granulation. However, we prefer not to draw any conclusions from these due to the many possible reasons why image power spectra can fall off as power laws. Whether in this case, this is indeed due to preferred widths or to sharp edges between bright and dark structures, scale invariance, turbulence, or other random processes, we cannot tell from these investigations. Finding typical scales for penumbral filament widths, if such typical scales do exist, requires a more direct method of pattern recognition.

5. Summary

Keeping in mind that we have studied only one specific penumbra, we summarize our results as following.

From inspection of the images, it is clear that sunspot penumbrae consist of filaments also at a resolution better than 100 km. They are likely to continue at even smaller scales, since there are still unresolved filaments which must have widths smaller than 80 km. The fine structure along the filaments is limited so that filaments do not seem to be composed of chains of aligned penumbral grains. At this resolution, penumbral grains have internal structure and look like they are crossed by narrow dark structures.

We calculated spatial power spectra of the penumbra and compared the results with the earlier work of Sánchez Almeida & Bonet (1998) and Sütterlin (2001) who studied sunspot penumbrae at lower spatial resolution. Since our PD procedure to correct the G-band images for seeing effects is based on a truncated expansion of the wavefront, we estimated the effect of high order aberrations on the power spectra. We conclude that the correction that might be applied to the power spectra is too low for the resulting penumbral power spectrum to be flat, in conflict with the results of Sánchez Almeida & Bonet (1998), but in agreement with Sütterlin (2001). Atmospherically scattered stray light that was not corrected for in the methods of Sütterlin (2001) and ourselves, is unlikely to affect the power spectra at small spatial scales.

Sütterlin (2001) reported an enhancement in spatial power around 0.″35 in penumbral power spectra which might point to a preferred width of penumbral filaments. In our penumbral power spectra from more highly resolved observations, we do not find any enhancement in power at these scales. A preliminary estimate is that the penumbral power spectrum in the G-band approximately fits a power law $\nu^{-4.0}$, slightly steeper than active granulation that falls off like $\nu^{-3.6}$.

We finally remark that power spectra are not very useful for finding typical sizes because power at high spatial frequencies does not necessarily come from small structures.

Acknowledgements. The Swedish 1-m Solar Telescope is operated on the island of La Palma by the Royal Swedish Academy of Sciences in the Spanish Observatorio del Roque de los Muchachos of the Instituto de Astrofísica de Canarias. We thank Pit Sütterlin for providing us with his DOT images. Jorge Sánchez Almeida is thanked for valuable comments on the manuscript. Eric Stevens at Eastman Kodak calculated the model detector MTFs for the KAF 1600 and KAF 4200 CCDs.

Appendix: Noise correction for power spectra

We write the Fourier transform of data frame number n as

$$D_n = FS_n + N_n = G_n + N_n, \tag{1}$$

where S_n is the corresponding OTF, and N_n is a realization of additive Gaussian white noise, respectively. F is the object and G_n is the object convolved with the atmospheric and instrumental PSF, i.e., a noiseless image.

Normally, the deconvolution of images based on instrumental MTFs and PD estimated atmospheric OTFs involves a noise filter. However, for the purpose of calculating power spectra, the estimated object is calculated simply with a multi-frame inverse filter operation,

$$\widehat{F} \approx \frac{\sum_n (G_n + N_n)\widehat{S}_n^*}{\sum_n |\widehat{S}_n|^2}, \tag{2}$$

where a $\widehat{\cdot}$ denotes an estimated quantity and a $*$ used as a superscript denotes a complex conjugate. The summation is over the (four) focused images in a PDS data set (we exclude the diversity out-of-focus images from the final deconvolution). Equation (2) is a good approximation at low spatial frequencies, but at high frequencies it is dominated by amplified noise. While this is usually filtered out for viewing, the filtering does distort high frequency power and is therefore not desirable when we are interested in the power spectrum itself. The power spectrum of the inverse filtered data takes the form

$$P = \frac{\sum_n (G_n + N_n)\widehat{S}_n^* \sum_m (G_m^* + N_m^*)\widehat{S}_m}{\sum_n |\widehat{S}_n|^2 \sum_m |\widehat{S}_m|^2}. \tag{3}$$

We now want to remove the contribution from the noise. The real noise, N_n, is unknown but we can base the correction on the expected noise power. The noise and the solar features are uncorrelated, so when calculating the expectance value, cross terms do not contribute. Also, noise in different frames is independent so $\langle N_n N_m \rangle \propto \delta_{nm}$. We get

$$\langle P \rangle = \frac{\sum_{n,m} G_n G_m^* \widehat{S}_n^* \widehat{S}_m}{(\sum_n |\widehat{S}_n|^2)^2} + \frac{\sum_n \langle |N_n|^2 \rangle |\widehat{S}_n|^2}{(\sum_n |\widehat{S}_n|^2)^2}, \tag{4}$$

where, for $\widehat{S}_n \equiv S_n$, the first fraction reduces exactly to the wanted object power spectrum, $|F|^2$, and the second fraction is the noise correction term that should be subtracted. The noise level, $\langle |N_n|^2 \rangle$, is measured by averaging outside the diffraction limit and in areas unaffected by the discontinuity caused by wrap-around of the finite subfield.

For the MTF filtered data, the summations are over a single frame only, and the square of the theoretical MTF can be substituted for $|\widehat{S}_n|^2$. The correction term then simplifies to $\langle |N|^2 \rangle / \mathrm{MTF}^2$.

References

Berger, T. E., Schrijver, C. J., Shine, R. A., et al. 1995, ApJ, 454, 531
Bonet, J. A., Ponz, J. D., & Vázquez, M. 1982, Sol. Phys., 77, 69
Bonet, J. A., Sobotka, M., & Vázquez, M. 1995, A&A, 296, 241
Chae, J., Yun, H. S., Sakurai, T., & Ichimoto, K. 1998, Sol. Phys., 183, 229
Field, D. J. 1987, J. Opt. Soc. Am. A, 4, 2379
Gonsalves, R. A. 1982, Opt. Eng., 21, 829
Löfdahl, M. G. 2002, in Image Reconstruction from Incomplete Data II, ed. P. J. Bones, M. A. Fiddy, & R. P. Millane, Proc. SPIE, 4792, 146
Löfdahl, M. G., Berger, T. E., & Seldin, J. H. 2001, A&A, 377, 1128
Löfdahl, M. G., Berger, T. E., Shine, R. A., & Title, A. M. 1998, ApJ, 495, 965
Löfdahl, M. G., & Scharmer, G. B. 1994, A&AS, 107, 243
Löfdahl, M. G., & Scharmer, G. B. 2003, in Innovative Telescopes and Instrumentation for Solar Astrophysics, ed. S. Keil, & S. Avakyan, Proc. SPIE, 4853, 567
Martínez Pillet, V. 2000, A&A, 361, 734
Muller, R. 1973a, Sol. Phys., 29, 55
Muller, R. 1973b, Sol. Phys., 32, 409
Muller, R. 1992, in Sunspots. Theory and Observations, NATO ASIC Proc., 375, 175
Muller, R., & Roudier, T. 1984, Sol. Phys., 94, 33
Müller, D., Schlichenmaier, R., Steiner, O., & Stix, M. 2002, A&A, 393, 305
Nisenson, P., & Barakat, R. 1987, J. Opt. Soc. Am. A, 4, 2249
Noll, R. J. 1976, J. Opt. Soc. Am., 66, 207
Nordlund, A., Spruit, H. C., Ludwig, H.-G., & Trampedach, R. 1997, A&A, 328, 229
Parker, E. N. 1992, in NATO ASIC Proc. 375: Sunspots. Theory and Observations, 413
Paxman, R. G., Schulz, T. J., & Fienup, J. R. 1992a, J. Opt. Soc. Am. A, 9, 1072
Paxman, R. G., Schulz, T. J., & Fienup, J. R. 1992b, in Technical Digest Series, Vol. 11, Signal Recovery and Synthesis IV, Optical Society of America, 5–7
Roddier, N. 1990, Opt. Eng., 29, 1174
Sánchez Almeida, J. 1998, ApJ, 497, 967
Sánchez Almeida, J., & Bonet, J. A. 1998, ApJ, 505, 1010
Scharmer, G. B. 1989, in Solar and Stellar Granulation, ed. R. J. Rutten, & G. Severino (Kluwer Academic Publisher), 161–171
Scharmer, G. B., Bjelksjö, K., Korhonen, T. K., Lindberg, B., & Pettersson, B. 2003a, in Innovative Telescopes and Instrumentation for Solar Astrophysics, ed. S. Keil, & S. Avakyan, Proc. SPIE, 4853, 341
Scharmer, G. B., Dettori, P., Löfdahl, M. G., & Shand, M. 2003b, in Innovative Telescopes and Instrumentation for Solar Astrophysics, ed. S. Keil, & S. Avakyan, Proc. SPIE, 4853, 370
Scharmer, G. B., Gudiksen, B. V., Kiselman, D., Löfdahl, M. G., & Rouppe van der Voort, L. H. M. 2002, Nature, 420, 151
Schlichenmaier, R. 2002, Astron. Nachr., 323, 303
Schlichenmaier, R., Jahn, K., & Schmidt, H. U. 1998a, ApJ, 493, L121
Schlichenmaier, R., Jahn, K., & Schmidt, H. U. 1998b, A&A, 337, 897
Sobotka, M. 1997, in 1st Advances in Solar Physics Euroconference. Advances in Physics of Sunspots, ASP Conf. Ser., 118, 155
Sobotka, M., Brandt, P. N., & Simon, G. W. 1999, A&A, 348, 621
Sobotka, M., & Sütterlin, P. 2001, A&A, 380, 714
Solanki, S. K., & Montavon, C. A. P. 1993, A&A, 275, 283
Stevens, E. G., & Lavine, J. P. 1994, IEEE transactions on electronic devices, 41, 1753
Sütterlin, P. 2001, A&A, 374, L21
Thomas, J., Weiss, N., Tobias, S., & Brummell, N. 2002, Nature, 420, 390
Thomas, J. H., & Weiss, N. O., eds. 1992, NATO ASIC Proc., 375, Sunspots. Theory and Observations
Tritschler, A., & Schmidt, W. 2002, A&A, 388, 1048